


Article

Effects of Empirical Dispersion Energy on the Geometrical Parameters and Relative Energy of a Salicylideneaniline Molecular Switch in the Solid State

Jean Quertinmont ¹ , Tom Leyssens ², Johan Wouters ¹ and Benoît Champagne ^{1,*} 

¹ Unité de Chimie Physique Théorique et Structurale, Namur Institute of Structured Matter, University of Namur, 61 Rue de Bruxelles, B-5000 Namur, Belgium; jean.quertinmont@unamur.be (J.Q.); johan.wouters@unamur.be (J.W.)

² Institute of Condensed Matter and Nanosciences, Université Catholique de Louvain, 1 Place Louis Pasteur, B-1348 Louvain-La-Neuve, Belgium; tom.leysens@uclouvain.be

* Correspondence: benoit.champagne@unamur.be; Tel.: +32-81-724554

Received: 12 February 2018; Accepted: 6 March 2018; Published: 8 March 2018

Abstract: The geometries of the enol (E) and keto (K) forms of a crystalline salicylideneaniline molecular switch, (E)-2-methoxy-6-(pyridine-3-yliminomethyl)phenol (PYV3), have been determined using periodic density functional theory (DFT) calculations with a variety of exchange-correlation functionals (XCFs). They are compared to X-ray diffraction (XRD) data as well as to geometries obtained using empirical dispersion energy in the form of the second iteration of Grimme's scheme, either with its original parameters (DFT-D2) or with parameters revised for the solid state (DFT-D*). Using DFT, a good agreement with experiment on the unit cell parameters is obtained with the PBEsol, PBEsol0, and ω B97X XCFs. DFT-D2 contracts the unit cell too much with all considered XCFs, whereas DFT-D* lessens this effect thus allowing B3LYP, PBE, and PBE0 to achieve reasonable agreement with respect to XRD data. When considering molecular geometries, both DFT and DFT-D* have a similar effect on the bond lengths, both systematically underestimating (overestimating) the length of the single (double) bonds (within 0.003 Å), as well as on valence angles attaining differences of 2° with respect to XRD data. The errors on the torsion angles are less spread out with DFT-D* (averaging 1°) than DFT for which only PBEsol, PBEsol0, and ω B97X perform well. Finally, the relative keto–enol energies, ΔE_{KE} , have been calculated, showing that the inclusion of dispersion energy stabilizes the keto form more than it does the enol form. This results in the PBE and PBEsol XCFs wrongly predicting the keto form as the most stable form.

Keywords: salicylideneaniline molecular crystals; solid state geometry optimizations; dispersion energy corrections

1. Introduction

Thermochromic and photochromic compounds have been extensively studied and still attract a lot of attention as they have many potential applications [1–8]. With the focus moving from the liquid phase to the more practical solid one, computational methods well set for quantum calculations of inorganic solids are now being challenged by the molecular crystalline state. In particular, accurate description of the intramolecular parameters (defined by the fractional coordinates of the asymmetric unit) and the intermolecular ones (defined by the unit cell parameters) is required as a starting point for the prediction and study of their properties. Density functional theory (DFT) was recently shown to be an efficient tool granted that the appropriate exchange-correlation functional (XCF) is used [9,10]. In [9], Ruggiero and co-workers assessed the reliability of a range of XCFs for the optimization of

three pyridine carboxylic acid crystals and they highlighted the performances of ω B97X [11]. In [10], we showed the effectiveness of three XCFs (HSEsol [12], PBEsol0, and ω B97X [11]) in optimizing the molecular and crystal structures of three salicylideneanilines. Still, with respect to the XCFs used so far, a more precise description of the solid state can be obtained by modifications to the DFT energy by adding London dispersion interactions (Equation (1)) in the form of empirical terms as proposed by Grimme [13].

$$E_{\text{DFT-D}} = E_{\text{DFT}} + E_{\text{disp}} \quad (1)$$

where E_{disp} is the empirical dispersion energy. We consider the second iteration of this scheme, containing less empirical parameters than the first one, and known as DFT-D2. The general expression for E_{disp} reads

$$E_{\text{disp}} = -s_6 \sum_{\mathbf{g}} \sum_{ij} f_{\text{dmp}}(R_{ij,\mathbf{g}}) \frac{C_6^{ij}}{R_{ij,\mathbf{g}}^6}, \quad (2)$$

with the first summation running over all lattice vectors, \mathbf{g} , and the second one running over all atom pairs (excluding the self-interaction case, when $i = j$ for $\mathbf{g} = 0$). s_6 is a scaling factor depending on the functional, $C_6^{ij} = \sqrt{C_6^{ii}C_6^{jj}}$ is the dispersion coefficient for the ij pair, $R_{ij,\mathbf{g}}$ is the distance between atom i in the reference cell ($\mathbf{g} = 0$) and atom j in cell \mathbf{g} , and $f_{\text{dmp}}(R_{ij,\mathbf{g}})$ is a dampening function specified as

$$f_{\text{dmp}}(R_{ij,\mathbf{g}}) = \left[1 + e^{-d\left(\frac{R_{ij,\mathbf{g}}}{R_{vdw}} - 1\right)} \right]^{-1} \quad (3)$$

In the latter expression, R_{vdw} is the sum of the van der Waals radii of atoms i and j and d defines the steepness of the function. Since this scheme was parameterized for clusters, Ugliengo and coworkers proposed to scale the coefficients published by Grimme in order to better describe the dispersion energy in molecular crystals, leading to DFT-D* (these modifications include a decrease of the scaling factor by a factor 0.95 and a scale up of the atomic van der Waals radii by 1.05 and 1.30 for heavy and hydrogen atoms, respectively) [14]. This modification results in smaller dispersion energies.

In this paper, we evaluate the effects of these additional empirical dispersion energy terms (DFT-D2 and DFT-D*) on the optimized geometrical parameters of a molecular crystal from the salicylideneaniline family, (E)-2-methoxy-6-(pyridine-3-yliminomethyl)phenol (PYV3, Figure 1). This compound is in fact a molecular switch that can commute between an enol (E) and a keto (K) form, allowing in parallel to evaluate the effect on the relative energy of these two forms. The theoretical structures obtained with DFT-D2 and DFT-D* XCFs are compared to X-ray diffraction (XRD) data as well as to those results obtained with more traditional DFT functionals [10]. This paper is organized as follows: Section 2 summarizes the key computational aspects (additional details can be found in [10]), whereas Section 3 presents and discusses the results before conclusions are drawn in Section 4.

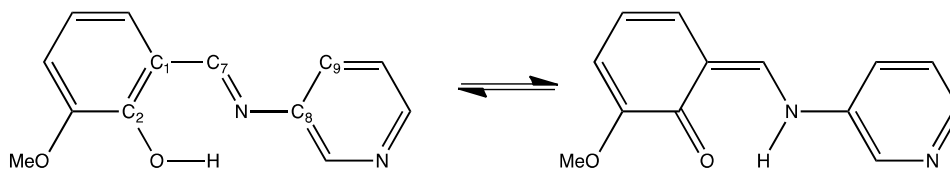


Figure 1. Structure and keto–enol equilibrium of the studied salicylideneaniline: (E)-2-methoxy-6-(pyridine-3-yliminomethyl)phenol (PYV3). Key bonds and atoms characterizing the geometries are highlighted on the enol structure.

2. Computational Aspects

Calculations were performed with the Crystal14 package [15] using various XCFs: B3LYP [16], PBE [17], PBE0 [18], PBEsol [19], PBEsol0, and ω B97X [11] with and without including London

dispersion interactions. This is achieved by using Grimme's empirical dispersion corrections [13]. First, the original parameters were employed (DFT-D2), followed by those revised for the crystalline state (DFT-D*) [14]. The steepness d of the damping function was set to 20 and a cutoff distance of 25 Å was set for the lattice summations. The default integration grid was used; the truncation criteria for the bielectronic integrals (TOLINTEG keyword) were set to 8 8 8 8 16 for all XCFs, except for ω B97X where 7 7 7 7 16 was used; the maximum order of the shell multipole is kept to the default, as well as all convergence criteria for both the SCF cycles and the optimization. A Monkhorst-Pack shrinking factor of 6 was used, yielding 64 integration points in the irreducible Brillouin zone. Pople's 6-31G(d,p) basis set was used as taken from Basis Set Exchange [20,21].

3. Results and Discussion

3.1. Crystal Structures and Molecular Geometries

First, we start by comparing the optimized structures of PYV3 obtained using the three 'levels' of DFT, i.e., DFT, DFT-D2, and DFT-D*, and a selection of XCFs to X-ray diffraction (XRD) data obtained at 108 K. According to the electron density map and to key bond lengths, at this temperature molecules are under the enol form [22,23]. The focus is first set on the unit cell volumes (Table 1) and the unit cell parameters (Figure 2), then on key bond lengths and angles (Figures 3 and 4). Although we compare the calculated pure enol form at 0 K to the XRD structure, the experimental variations between the low and room temperature structures (a ~3% increase of volume, up to 0.01 Å differences in bond lengths, and 0.6° in angles) are well within the accuracy that can be obtained by computations.

Considering the unit cell volume, the use of the reference DFT XCFs yield either large errors with respect to XRD data (B3LYP 17%, PBE 12%, and PBE0 11%) or errors within a satisfying range ($\leq 2\%$): PBEsol < -1%, PBEsol0 < -1%, ω B97X < -2%. Addition of empirical dispersion energy overall leads to smaller unit cell volumes. In the case of DFT-D2, the unit cells are over-contracted, meaning relative errors ranging from -15 to -8%, while the DFT-D* results tone down this effect to yield volumes either in closer agreement with the experimental values for those XCFs performing poorly with DFT (B3LYP -5%, PBE -3%, and PBE0 -6%), or still over-contracting the unit cell volume for PBEsol, PBEsol0, and ω B97X (errors between -11.6 and -11.2%).

Table 1. Differences of unit cell volume [$\Delta V = V(E) - V(\text{XRD})$, in Å³, and $\Delta V/V = \Delta V/V(\text{XRD})$, in %] as calculated with different XCFs and models for PYV3. The 6-31G(d,p) basis set was used for all calculations.

Method	DFT	DFT-D2	DFT-D*
B3LYP	189.0 (17.2%)	-112.9 (-10.3%)	-52.3 (-4.8%)
PBE	129.4 (11.8%)	-89.3 (-8.1%)	-36.2 (-3.3%)
PBE0	117.3 (10.7%)	-112.3 (-10.5%)	-61.1 (-5.6%)
PBEsol	-5.2 (-0.5%)	-169.3 (-15.4%)	-122.9 (-11.2%)
PBEsol0	-7.0 (-0.6%)	-170.5 (-15.5%)	-127.2 (-11.6%)
ω B97X ¹	-21.9 (-2.0%)	-163.4 (-14.9%)	-124.9 (-11.4%)

¹ TOLINTEG = 777716.

Figure 2 shows the unit cell parameter (a , b , and c) variations with respect to XRD data. When using conventional DFT XCFs (B3LYP, PBE, and PBE0), variations on the unit cell parameters, all are positive (except for PBE) and larger than 3% (Figure 2a). On the other hand, when using XCFs optimized for the solid state (PBEsol and PBEsol0) as well as ω B97X the differences with respect to XRD data are smaller than 3% and not systematically positive (leading to error cancellation on the estimated unit cell volume, e.g., for PBEsol: the error on a , -2.7%, is partially cancelled by the one on b , 1.9%, while c is fairly accurately estimated, 0.5%).

In the case of DFT-D* (Figure 2b) the a parameter is strongly underestimated (errors between -6 and -10%) for all XCFs while the errors on b are positive (except for ω B97X) allowing for error

compensation on the volume when c is accurate (between -0.8 and 0.4%): B3LYP, PBE, and PBE0. This explains why the volume is closer to experiment with these three functionals (-5.6 to -3.3%) than with PBEsol, PBEsol0, and ω B97X (-11.6 to -11.2%). Indeed, for the latter XCFs, the errors on the a and c parameters are both negative (-2.3 to -3.1%) and are not compensated by the errors on b . Finally, the DFT-D2 model, Figure 2c, results in strong and systematic underestimations of all parameters, ranging from -2.5 to -7.7% . A distinction can be made for the a parameter as determined with B3LYP, PBE, and PBE0 for which the error is smaller, $\sim 3\%$, than with the other XCFs, $\sim 7\%$, while the errors for b and c are similar among the XCFs. This results in B3LYP, PBE, and PBE0 volumes that are slightly better than the PBEsol, PBEsol0, and ω B97X ones.

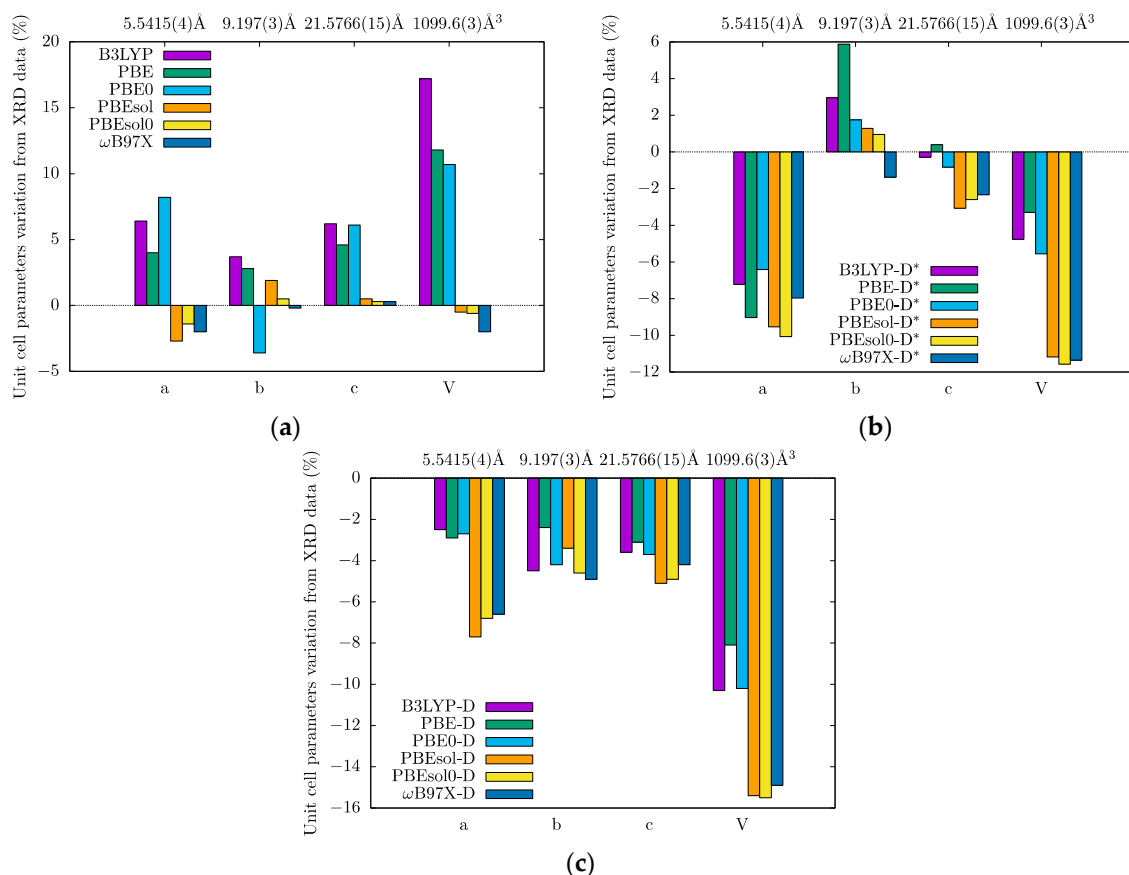


Figure 2. Differences (in %) between the optimized unit cell parameters and the XRD values as a function of the XCF, $\Delta = [X(\text{Calc.}) - X(\text{XRD})]/X(\text{XRD})$: (a) with DFT; (b) with DFT-D*; (c) with DFT-D2. The XRD values are given on the top of each figure. The 6-31G(d,p) basis set was used for all calculations.

Accurate unit cell parameters constitute a good starting point for further investigation of thermodynamic or optical properties, at least as long as the bond lengths and angles are also accurately modelled. Figure 3 shows key bond length variations with respect to XRD data along the O-C₂-C₁-C₇-N-C₈ path (Figure 1). Moreover, two bond length ratios are considered, the N- and C-ratios, which describe the π -conjugation and are defined as

$$\text{C-ratio} = d(\text{C}_1 - \text{C}_7)/d(\text{C}_2 = \text{C}_1), \quad (4)$$

$$\text{N-ratio} = d(\text{N} - \text{C}_8)/d(\text{C}_7 = \text{N}), \quad (5)$$

The comparison to experiment is not presented for DFT-D2 since we just showed its poor reliability for unit cell parameters. Figure 3a, for DFT, and Figure 3b, for DFT-D*, highlight the systematic underestimation (overestimation) of the single (double) bond lengths, with the exception of C₁-C₇ and C₇=N with ω B97X. Still, in the worst case scenarios, these errors are smaller than 0.025 Å and generally of the order of 0.01 Å. This results in N-/C-ratios that are slightly underestimated, especially in the case of the two GGA XCFs, PBE and PBEsol, whereas the ω B97X's ratios are slightly overestimated. The DFT-D* results are extremely similar to the DFT ones since the differences do not exceed 0.003 Å. This affects the ratios by about the same amount.

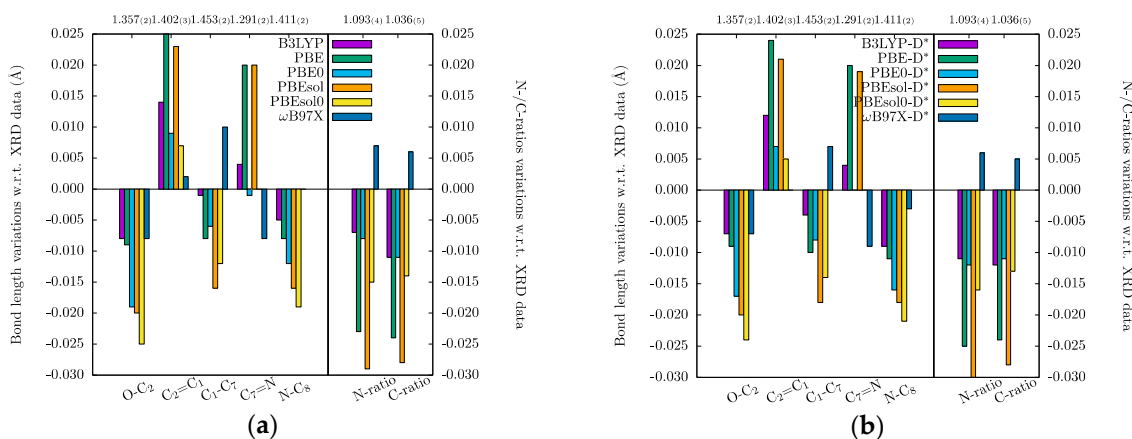


Figure 3. Differences between the bond lengths of the optimized structure and of the XRD data as a function of the XCF, $\Delta = [d(\text{DFT}) - d(\text{XRD})]$: (a) with DFT; (b) with DFT-D*. The XRD values are given on the top of each figure. The 6-31G(d,p) basis set was used for all calculations.

As for the valence and torsion angles, variations with respect to XRD data are presented in Figure 4 for two valence angles (C₁-C₇-N and C₇-N-C₈), the three torsion angles involving the C₇=N bond (C₂-C₁-C₇-N, C₁-C₇-N-C₈, and C₇-N-C₈-C₉), one torsion angle associated with the H-bond (C₂-O-N-C₇), and one torsion angle describing the global torsion of the molecule (C₂-C₁-C₈-C₉). As before, only DFT and DFT-D* results are discussed (Figure 4a,b, respectively). The absolute errors on the valence angles are within a $[-2^\circ; 2^\circ]$ range for all XCFs using both types of DFT ($\sim 2\%$ of relative error). For the torsion angles, in the case of DFT without dispersion, they are systematically underestimated, except for ω B97X. Furthermore, the error on the molecular torsion angle C₂-C₁-C₈-C₉ and, to a smaller extent on the angle C₇-N-C₈-C₉, is quite large for those XCFs that poorly perform for the unit cell parameters (with errors ranging between -5.7° and -10.5° for B3LYP, PBE, and PBE0). For the other XCFs (PBEsol, PBEsol0, and ω B97X), the deviations are much smaller: -3.1° , -3.1° , and -1.0° , respectively. This highlights the key role of the torsion angles on the unit cell parameters or, in other words, their interdependence. It is however difficult to say whether the error on the torsion angles drives the error on the unit cell or vice versa.

When using the DFT-D* model, the amplitude of the errors is greatly reduced compared to standard DFT, in particular for B3LYP, PBE, and PBE0. Note that the scale of Figure 4a for DFT goes from -12 to 4° while that of Figure 4b for DFT-D*, from -2 to 4° . For DFT-D*, the errors on the torsion angles are mainly positive, except for the C₁-C₇-N-C₈ angle. For the important molecular torsion (C₂-C₁-C₈-C₉), the error is around 1° for all XCFs, except for PBE0 ($<1^\circ$) and ω B97X (2°), which is on par with the errors of PBEsol, PBEsol0, and ω B97X with DFT for the same angle. Accurate molecular torsions are obtained in parallel to accurate unit cell parameters.

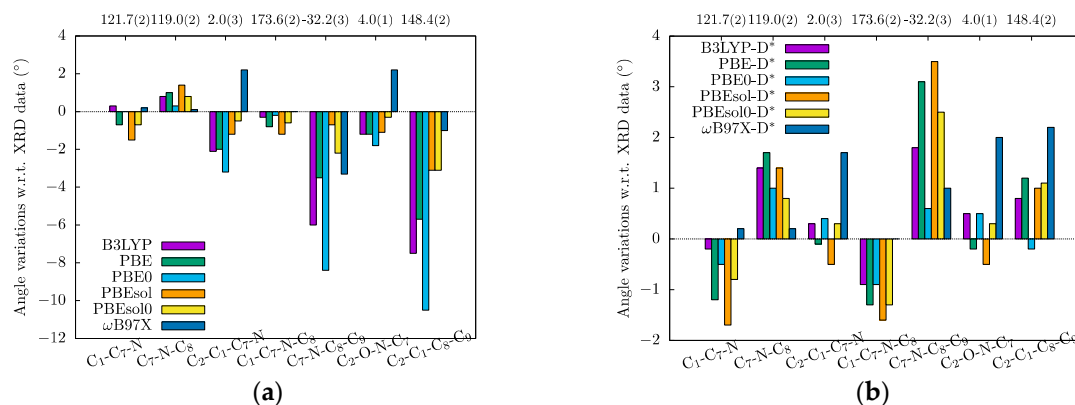


Figure 4. Differences between the angles of the optimized structure and of the XRD data as a function of the XCF, $\Delta = [a(\text{DFT}) - a(\text{XRD})]$: (a) with DFT; (b) with DFT-D*. The XRD values are given on the top of each figure. The 6-31G(d,p) basis set was employed for all calculations.

3.2. Keto–Enol Energies

After investigating the geometrical structures, we now turn to studying the effect of the methods used on the relative energy of the keto and enol forms (Table 2). Experimentally, XRD measurements show only the enol form of PYV3 to be present both at low and room temperatures. This highlights the fact that the enol form (E) is more stable than the keto one (K). The relative energy difference, $\Delta E_{KE} = E(K) - E(E)$, is thus expected to be positive. Table 2 shows the relative energies computed with the selected XCFs. Although ΔE_{KE} varies significantly depending on the XCF, all DFT values are positive, ranging from 1 to 13 kJ/(mol of asymmetric unit), in agreement with experiment. Addition of dispersion energy has a more important stabilizing effect on the keto form compared to the enol one, leading overall to less positive ΔE_{KE} values, if not negative ones like in the case of PBE and PBESol [−2.5 and −2.7 kJ/(mol asym. unit) for DFT-D2 and −1.3 and −1.9 kJ/(mol asym. unit) for DFT-D*, respectively]. Since we know from experiment that ΔE_{KE} is positive, these two XCFs are not considered any further. DFT-D2 values, ranging from 2.7 to 10.2 kJ/(mol asym. unit), vary little from the DFT-D* ones (ranging from 3.4 to 9.9 kJ/(mol asym. unit)). Still, as expected, the dispersion energies obtained with DFT-D2 are larger than with DFT-D*, which favors the keto form hence decreasing the relative energy difference ΔE_{KE} (with the exception of ωB97X). The energy difference can be used to analyze the K/E Boltzmann distributions at 298.15 K to further quantify the effects of the dispersion energy. In the case of ωB97X, barely no change is observed, with the keto population increasing from 1% with DFT to 2% with DFT-D2/D*. The effects are much larger for the other functionals, and they correspond to at least a 10% increase of the keto form upon adding dispersion, i.e., from 1 to 14% for PBE0, from 3 to 25% for B3LYP, and from 5 to 20% for PBESol0.

Table 2. Keto–enol energy differences [$\Delta E_{KE} = E(K) - E(E)$, in kJ/(mol asym. unit)] as calculated with different XCFs for PYV3. The percentage of keto calculated using Boltzmann’s distribution at 298.15 K is given in parentheses. The 6-31G(d,p) basis set was used in all calculations.

Method	DFT	DFT-D2	DFT-D*
B3LYP	8.3 (3%)	2.7 (25%)	3.4 (20%)
PBE	2.6 (26%)	−2.5 (73%)	−1.3 (63%)
PBE0	11.0 (1%)	4.5 (14%)	5.3 (11%)
PBESol	1.0 (40%)	−2.7 (75%)	−1.9 (68%)
PBESol0	7.1 (5%)	3.4 (20%)	4.0 (17%)
ωB97X ¹	12.9 (1%)	10.2 (2%)	9.9 (2%)

¹ TOLINTEG = 7 7 7 7 16.

4. Conclusions

Density functional theory has been challenged for the geometry optimization of molecular switches in their solid crystalline state. By performing comparisons with X-ray diffraction (XRD) data, a recent contribution [10] has demonstrated that HSEsol [12], PBEsol0, and ω B97X [11] can already be effective but, in this work, we investigated whether the addition of empirical dispersion energy, as proposed by Grimme [13], could further improve these results. First, we have shown that the use of the original dispersion parameters (DFT-D2) over-contracts the unit cell for the selected XCFs (B3LYP [16], PBE [17], PBE0 [18], PBEsol [19], PBEsol0, and ω B97X). On the other hand, the down-scaled parameters proposed for the solid state (DFT-D*) [14] decrease this effect so that the B3LYP, PBE, and PBE0 XCFs achieve a rather good agreement with XRD data when considering the unit cell volume, though, mostly due to error compensations. Looking at the molecular geometries, the main conclusions are: (i) inclusion of dispersion energy has almost no effect on the bond lengths, though systematically underestimating (overestimating) the length of the single (double) bonds, with the maximum difference between DFT and DFT-D* attaining 0.003 Å; (ii) the valence angles are also barely affected when using DFT-D* compared to DFT with relative errors with respect to XRD data of 2% or less in both cases; and (iii) in the case of the torsion angles, the use of DFT-D* XCFs improves the results since the variations with respect to XRD data are less spread out. The average errors with DFT-D* are of the order of 1° whereas with DFT, only the PBEsol, PBEsol0, and ω B97X XCFs perform well. This means that an accurate description of the unit cell parameters leads to accurate molecular torsions but that accurate molecular torsions do not constitute a sufficient condition to fully describe the intermolecular interactions, and to reproduce the XRD unit cell. Finally, for all XCFs, the relative keto–enol energy differences ΔE_{KE} have been calculated, showing that the inclusion of dispersion stabilizes the keto form more than the enol form. As a consequence, the PBE and PBEsol XCFs incorrectly predict the keto form to be the most stable. The other functionals, with exception of ω B97X, predict a decrease of ΔE_{KE} but the overall value remains positive. Overall, these results show PBEsol0 and ω B97X XCFs to be reliable in predicting molecular crystal structures and that there is no clear advantage of using empirical energy dispersion corrections as originally proposed [13] or later reparameterized [14] for solids.

Acknowledgments: This work was carried out thanks to funding of “Actions de Recherche Concertées”(ARC) de la Direction générale de l’Enseignement non obligatoire et de la Recherche scientifique—Direction de la Recherche scientifique—Communauté française de Belgique, under convention no.15/20-068. This research used resources of the “Plateforme Technologique de Calcul Intensif (PTCI)” (<http://www.ptci.unamur.be>) located at the University of Namur, Belgium, which is supported by the F.R.S.-FNRS under the convention no. 2.5020.11. The PTCI is a member of the “Consortium des Équipements de Calcul Intensif (CÉCI)” (<http://www.ceci-hpc.be>). The authors thank Andrea Carletta for our discussions.

Author Contributions: Benoît Champagne and Jean Quertinmont conceived the investigation. Jean Quertinmont performed all calculations and wrote the paper. All authors discussed the results and commented on the manuscript.

Conflicts of Interest: The authors declare no conflict of interest.

References

1. Crano, J.C.; Guglielmetti, R.J. *Organic Photochromic and Thermochromic Compounds*; Springer: New York, NY, USA, 1998.
2. Kawata, S.; Kawata, Y. Three-dimensional optical data storage using photochromic materials. *Chem. Rev.* **2000**, *100*, 1777–1788. [[CrossRef](#)] [[PubMed](#)]
3. Hadjoudis, E.; Mavridis, I.M. Photochromism and thermochromism of Schiff bases in the solid state: Structural aspects. *Chem. Soc. Rev.* **2004**, *33*, 579–588. [[CrossRef](#)] [[PubMed](#)]
4. Amimoto, K.; Kawato, T. Photochromism of organic compounds in the crystal state. *J. Photochem. Photobiol. C Photochem. Rev.* **2005**, *6*, 207–226. [[CrossRef](#)]
5. Feringa, B.L.; Browne, W.R. *Molecular Switches*, 2nd ed.; WILEY-VCH Press: Weinheim, Germany, 2011.
6. Antonov, L. *Tautomerism: Methods and Theories*; Wiley-VCH Press: Weinheim, Germany, 2013.

7. Antonov, L. *Tautomerism: Concepts and Applications in Science and Technology*; WILEY-VCH Press: Weinheim, Germany, 2016.
8. Padalkar, V.S.; Seki, S. Excited-state intramolecular proton-transfer (ESIPT)-inspired solid state emitters. *Chem. Soc. Rev.* **2016**, *45*, 169–202. [[CrossRef](#)] [[PubMed](#)]
9. Ruggiero, M.T.; Gooch, J.; Zubieta, J.; Korter, T.M. Evaluation of range-corrected density functionals for the simulation of pyridinium-containing molecular crystals. *J. Phys. Chem. A* **2016**, *120*, 939–947. [[CrossRef](#)] [[PubMed](#)]
10. Quertinmont, J.; Carletta, A.; Tumanov, N.A.; Leyssens, T.; Wouters, J.; Champagne, B. Assessing density functional theory approaches for predicting the structure and relative energy of salicylideneaniline molecular switches in the solid state. *J. Phys. Chem. C* **2017**, *121*, 6898–6908. [[CrossRef](#)]
11. Chai, J.-D.; Head-Gordon, M. Long-range corrected hybrid density functionals with damped atom-atom dispersion corrections. *Phys. Chem. Chem. Phys.* **2008**, *10*, 6615–6620. [[CrossRef](#)] [[PubMed](#)]
12. Schimka, L.; Harl, J.; Kresse, G. Improved hybrid functional for solids: The HSEsol functional. *J. Chem. Phys.* **2011**, *134*, 024116. [[CrossRef](#)] [[PubMed](#)]
13. Grimme, S. Semiempirical GGA-type density functional constructed with a long-range dispersion correction. *J. Comput. Chem.* **2006**, *27*, 1787–1799. [[CrossRef](#)] [[PubMed](#)]
14. Civalieri, B.; Zicovich-Wilson, C.M.; Valenzano, L.; Ugliengo, P. B3LYP augmented with an empirical dispersion term (B3LYP-D*) as applied to molecular crystals. *CrystEngComm* **2008**, *10*, 405–410. [[CrossRef](#)]
15. Dovesi, R.; Orlando, R.; Erba, A.; Zicovich-Wilson, C.M.; Civalieri, B.; Casassa, S.; Maschio, L.; Ferrabone, M.; De La Pierre, M.; D’Arco, P.; et al. CRYSTAL14: A program for the *ab initio* investigation of crystalline solids. *Int. J. Quantum Chem.* **2014**, *114*, 1287–1317. [[CrossRef](#)]
16. Stephens, P.J.; Devlin, F.J.; Chabalowski, C.F.; Frisch, M.J. Ab initio calculation of vibrational absorption and circular dichroism spectra using density functional force fields. *J. Phys. Chem.* **1994**, *98*, 11623–11627. [[CrossRef](#)]
17. Perdew, J.P.; Burke, K.; Ernzerhof, M. Generalized gradient approximation made simple. *Phys. Rev. Lett.* **1996**, *77*, 3865–3868. [[CrossRef](#)] [[PubMed](#)]
18. Adamo, C.; Barone, V. Toward chemical accuracy in the computation of NMR shieldings: The PBE0 model. *Chem. Phys. Lett.* **1998**, *298*, 113–119. [[CrossRef](#)]
19. Perdew, J.P.; Ruzsinszky, A.; Csonka, G.I.; Vydrov, O.A.; Scuseria, G.E.; Constantin, L.A.; Zhou, X.; Burke, K. Restoring the density-gradient expansion for exchange in solids and surfaces. *Phys. Rev. Lett.* **2008**, *100*, 136406. [[PubMed](#)]
20. Feller, D. The role of databases in support of computational chemistry calculations. *J. Comput. Chem.* **1996**, *17*, 1571–1586. [[CrossRef](#)]
21. Schuchardt, K.L.; Didier, B.T.; Elsethagen, T.; Sun, L.; Gurumoorthi, V.; Chase, J.; Li, J.; Windus, T.L. Basis Set Exchange: A community database for computational sciences. *J. Chem. Inf. Model.* **2007**, *47*, 1045–1052. [[CrossRef](#)] [[PubMed](#)]
22. Carletta, A.; Buol, X.; Leyssens, T.; Champagne, B.; Wouters, J. Polymorphic and isomorphic cocrystals of a n-salicylidene-3-aminopyridine with dicarboxylic acids: tuning of solid-state photo- and thermochromism. *J. Phys. Chem. C* **2016**, *120*, 10001–10008. [[CrossRef](#)]
23. Carletta, A.; Spinelli, F.; D’Agostino, S.; Ventura, B.; Chierotti, M.R.; Gobetto, R.; Wouters, J.; Grepioni, F. Halogen-bond effects on the thermo- and photochromic behaviour of anil-based molecular co-crystals. *Chem.-A Eur. J.* **2017**, *23*, 5317–5329. [[CrossRef](#)] [[PubMed](#)]

